Title

Instantaneous Amplitude and Frequency Dynamics of Coherent Wave Mixing in Semiconductor Quantum Wells

Author

Chemla, D.S.

Publication Date

1993-06-30

LBL-34433
UC-404

Lawrence Berkeley Laboratory
UNIVERSITY OF CALIFORNIA

Materials Sciences Division

To be presented at the International School of Physics
"Enrice Fermi" Varenna, Sullago de Como, Italy,
July 20–30, 1993, and to be published in the Proceedings

Instantaneous Amplitude and Frequency Dynamics of Coherent Wave Mixing in Semiconductor Quantum Wells

D.S. Chemla

June 1993

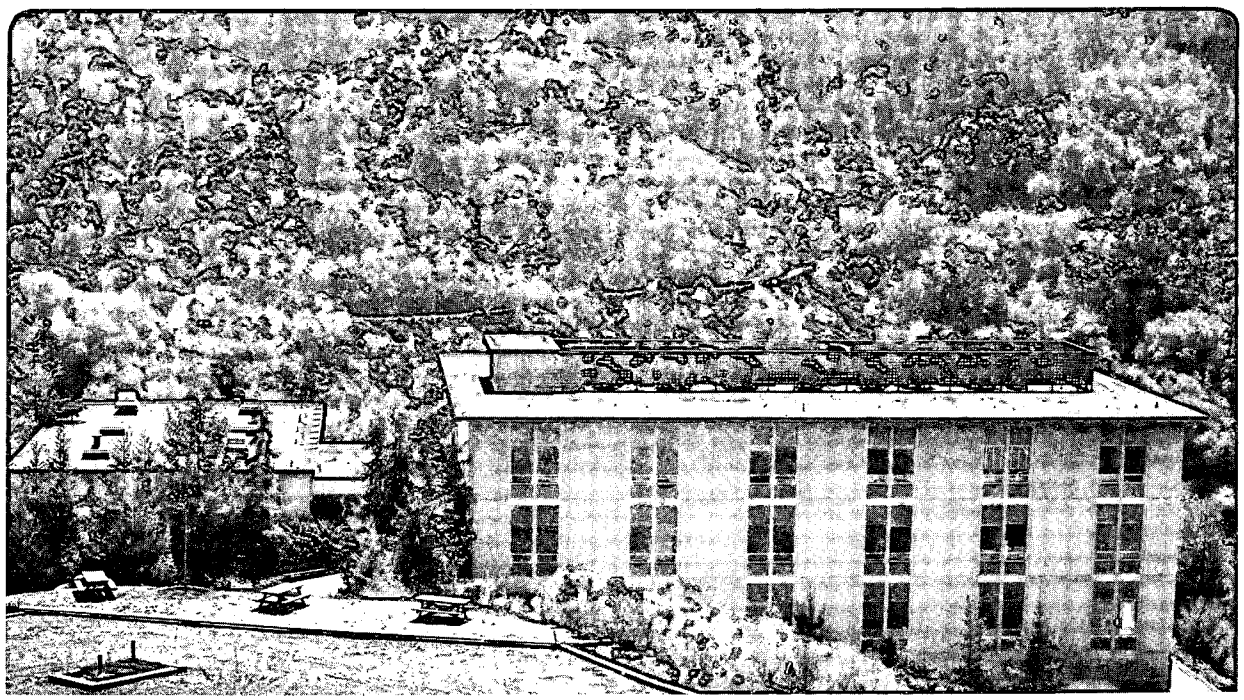

Prepared for the U.S. Department of Energy under Contract Number DE-AC03-76SF00098

DISCLAIMER

LBL-34433
UC-404

Instantaneous Amplitude and Frequency Dynamics of Coherent Wave Mixing in Semiconductor Quantum Wells

D.S. Chemla

Physics Department
University of California

and

Materials Sciences Division
Lawrence Berkeley Laboratory
University of California
Berkeley, CA 94720

June 1993

This work was supported by the Director, Office of Energy Research, Office of Basic Energy Sciences, Division of Materials Sciences, of the U.S. Department of Energy under Contract No. DE-AC03-76SF00098.

Instantaneous Amplitude and Frequency Dynamics of Coherent Wave Mixing in Semiconductor Quantum Wells

D.S. Chemla
Physics Department, University of California at Berkeley,
Material Sciences Division, Lawrence Berkeley Laboratory.

I) Introduction

The delocalized electronic excitations of semiconductors are very srongly coupled by the Coulomb interaction. When a semiconductor is excited close to the fundamental bandgap, this interaction renormalizes both the band energies and the Rabi frequency, which measures the coupling to the applied electromagnetic field.[1,2] The renormalizations are repectively proportional to the populations excited in the bands and to the interband polarization. They provide a source of optical nonlinearities which are qualitatively different from the nonlinearities of isolated atomic systems. Atomic nonlinearities originate from Pauli exclusion. They are present in all material systems, including semiconductors, and are essentially instantaneous. Conversely, the Coulomb many-body nonlinearities become visible only when the excitation has produced significant population and polarization densities. Their contribution to nonlinear optical response is delayed and dephased with respect to that due to the Fermi statistic. Therefore, many of the specificities of many-body nonlinearities appear in ultrashort pulse time-resolved nonlinear optical experiments.[3-10]

In this article we review recent investigations of the specific features of nonlinear optical processes in semiconductors. It is organized as follows. In Section II, we discuss the theory of coherent wave mixing in semiconductors. We emphasize the case where the

excitation is resonant with only one exciton state. In Section III we review our recent experimental investigations of the **amplitude and phase** of coherent wave-mixing resonant with quasi-2d excitons (X) in GaAs quantum wells (QW).[8,10] In Section IV we discuss these results and conclude.

II) Resonant Excitonic Nonlinearities in Semiconductors.

In this section we consider the case of a semiconductor resonantly excited at the lowest exciton state. Within this approximation, we wish to put the equations describing the time evolution of the exciton polarization and population, in a form simple enough to reveal directly the physics of the nonlinear optical response. We start from the usual two-band model of the semiconductor Bloch equation.[11] Neglecting the photon momentum, we only consider vertical transitions. In this case the density matrix, $\hat{n}(t)$, breaks into 2×2 blocks,

$$\hat{n}_k(t) = \begin{bmatrix} n_c(k) & \psi(k) \\ \psi^*(k) & n_v(k) \end{bmatrix} . \qquad (I.1)$$

where $n_{c,v}(k)$ are the electron populations in the conduction and valence bands, and $\psi(k)$ is the pair-amplitude which, as shown below, is proportional to the polarization (when it is possible to neglect the wavevector dependence of the interband dipole moment). The density matrix $\hat{n}(t)$ satisfies the Liouville equation;

$$\frac{\partial}{\partial t} \hat{n}_k(t) = -i[\, \hat{\varepsilon}_k(t) \,,\, \hat{n}_k(t) \,] + \frac{\partial}{\partial t} \hat{n}_k(t) \Big|_{relax} \qquad (I.2)$$

where the Hamiltonian matrix,

$$\hat{\varepsilon}_k(t) = \begin{bmatrix} \varepsilon_c(k) & 0 \\ 0 & \varepsilon_v(k) \end{bmatrix} + \begin{bmatrix} 0 & -\mu_k E \\ -\mu_k^* E^* & 0 \end{bmatrix} - \sum_{k'} V_{k,k'}\, \hat{n}_{k'} \qquad (I.3)$$

comprises of three contributions. The first one gives the bare-band energies, $\varepsilon_{c,v}(k) = \varepsilon_{c,v}^{(0)} + k^2/2m_{c,v}$. The second expresses the coupling of the interband dipole matrix element, μ_k, with the electromagnetic field E. Finally the third one describes the how the Coulomb potential, $V_{k,k'}$, couples states at different wavevector k. Dephasing is accounted for phenomenologically by the term, $\frac{\partial}{\partial t}\hat{n}_k(t)\,|_{relax}$.

From the diagonal and off-diagonal elements of $\hat{\varepsilon}$, one sees clearly how the Coulomb interaction renormalizes the energies and the Rabi frequency. The difference in these quantities when $V_{k,k'}$ is absent or present is,

$$\varepsilon_j(k) \rightarrow \varepsilon_j(k) - \sum_{k'} V_{k,k'}\, n_j(k'), \qquad (I.4a)$$

and

$$\mu_k E \rightarrow \mu_k E + \sum_{k'} V_{k,k'} \psi(k'). \qquad (I.4b)$$

For relaxed populations, the Coulomb terms in Eq.(I,4a) describe the well known "band gap renormalization". This equation accounts as well for the dynamic band-gap changes induced by coherent or transients populations. Similarly, the second term of Eq. (I.4b) describes the dynamic interaction involving polarization waves at different k. To bring out the effects of the nonequilibrium populations, we transform to the electron-hole representation, $n_c(k) \rightarrow n_e(k)$ and $n_v(k) \rightarrow 1 - n_h(k)$. From Eq.(I,1) we obtain the evolution equation of the populations;

$$(\frac{\partial}{\partial t} + \frac{\partial}{\partial t}|_{relax})n_e(k) = -(\frac{\partial}{\partial t} + \frac{\partial}{\partial t}|_{relax})n_h(k)$$

$$= 2\mathrm{Im}[\psi_k(\mu_k E + \sum_{k'} V_{k,k'}\psi(k'))^*], \qquad (I.5)$$

and of the pair-amplitude;

$$[i(\frac{\partial}{\partial t} + \frac{\partial}{\partial t}|_{relax}) - (E_g + \frac{k^2}{2m})]\psi(k) + \sum_{k'} V_{k,k'}\psi(k') = \qquad (I.6)$$

$$-(1 - n_e(k) - n_h(k))\,\mu_k E + 2\sum_{k'} V_{k,k'}(\,\psi(k)\,n(k') - n(k)\,\psi(k')\,).$$

In Eq. (I,6) the first driving term in the right hand side gives the nonlinearity due to the Fermi statistic, i.e. it accounts for the weakening of the coupling with the applied field due to Pauli exclusion. The second line expresses the Coulomb nonlinearity which corresponds to the exchange interaction between populations and polarizations at different wavevectors. A further and implicit source of nonlinearity is due to the dependence of the Coulomb potential itself on the electron and hole populations.

These equations are very complex and are usually solved numerically. Often the physical intuition is lost in the computation. In the case where a single excitonic resonance is optically excited, the population and polarization of this state dominate over that of the other states and, Eq.(I,5) and (I,6) can be greatly simplified.[13] First we Fourier transform these equations to r-space assuming that the interband dipole element is k-independent $\mu_k \rightarrow \mu$. Then, noting that, $\phi_\nu(r)$, the solutions of the exciton-Wannier equation in r-space,

$$[\frac{-1}{2m}\nabla_r^2 + V(r)]\,\phi_\nu(r) = E_\nu\,\phi_\nu(r), \qquad (I\text{-}7)$$

form an complete orthogonal basis set, we develop the polarization, $\psi(r)$, and populations, $n_e(r)$ and $n_h(r)$, on it.

$$\psi(r) = \sum_{\nu} \psi_\nu \, \phi_\nu(r) \tag{I-8a}$$

$$n_{(e,h)}(r) = \sum_{\nu} n_{(e,h)\nu} \, \phi_\nu(r) \tag{I-8b}$$

The "components", ψ_ν and $n_{(e,h)\nu}$, in the exciton-representation are not functions of r, they can be, however, functions of time. Their time evolution is found to be given by;

$$[i(\frac{\partial}{\partial t} + \Gamma_\lambda) - \Omega_\lambda]\psi_\lambda = -[L^3\phi^*_\lambda(r=0) - n_{e,\lambda} - n_{h,\lambda}]\mu E + \sum_{\mu\nu} V_{\lambda\mu\nu}(n_{e,\mu}\psi_\nu + n_{h,\mu}\psi_\nu) \tag{I-9a}$$

$$i(\frac{\partial}{\partial t} + \gamma_{e,\lambda})\, n_{e,\lambda} = i(\frac{\partial}{\partial t} + \gamma_{h,\lambda})\, n_{h,\lambda} = 2\mathrm{Im}[\,\mu E \psi^*_\lambda\,] + \sum_{\mu\nu} V_{\lambda\mu\nu}\,(\psi^*_\mu\psi_\nu - \psi_\mu\psi^*_\nu), \tag{I-9b}$$

where $\Omega_\lambda = E_g - E_\lambda$. We have defined the non-local matrix-potential, $V_{\lambda\mu\nu}$, by;

$$V_{\lambda\mu\nu} = \int d^3r' d^3r \, \phi^*_\lambda(r)\phi_\mu(r-r')V(r')\phi_\nu(r'), \tag{I-10}$$

and we have introduced the phenomenological damping rates of the exciton states; Γ_λ and $\gamma_{(e,h)\lambda}$. These equations show that the exciton states are equivalent to a set of two-level systems obeying Pauli exclusion and coupled by the non-local matrix potential $V_{\lambda\mu\nu}$. They are equivalent to the original Eq. (I-2).

To describe the case where only the lowest (1S) exciton state is resonantly excited, we retain only the terms for which $\lambda = \mu = \nu = 1S$. Henceforth we drop the index 1S to simplify the notation. We have, $\gamma_e \simeq \gamma_h \simeq T_1^{-1} = \gamma$ and, therefore, $n_h \simeq n_e = n$. Finally, in order to work with dimensionless quantities, we make a change of scale of all the variables according to recipe; $x \rightarrow x \times L^3\phi^*_{1S}(r=0)$ for $x = \psi$, n_e and n_h, and $V \rightarrow V = V/L^3\phi^*_{1S}(r=0)$. We obtain the equations describing the 1S-resonant excitation,

$$(\frac{\partial}{\partial t} + \gamma)\, n = -2\mathrm{Im}[\, \mu E \psi^*(r)\,] \qquad \text{(I-11a)}$$

$$\frac{\partial}{\partial t}\psi = -i(\Omega - i\Gamma)\psi + i\mu E \qquad \text{(I-11b)}$$

$$- i2n\,\mu E - 2iV\, n\psi$$

The first equation shows that the exciton state is simply populated by absorption exactly as in the case of a two level system (2LS). The second shows that the exciton behaves as a driven nonlinear oscillator. The first line describes the linear response of the oscillator driven by the applied field, while the two terms on the second line account the nonlinear response. The first nonlinear term originates from the Pauli-exclusion reduction of the exciton coupling with the electromagnetic field, $\mu E(t) \rightarrow (1 - 2n)\mu E(t)$. This term is, of course, always present and accounts for the atomic-type nonlinearities. The second nonlinear term is specific to dense media semiconductors and molecular crystals.[4-6,9,12] In semiconductors, it describes the Coulomb mediated exciton-exciton interaction which causes the coupling between populations and polarization waves within the medium. Furthermore, in a semiconductor, the Coulomb potential is sensitive to the non-equilibrium populations through dynamic screening, V itself is a function of n and ψ. This dependence provides an additional nonlinearity. We call the two nonlinear terms

the Phase Space Filling (PSF) and the exciton-exciton interaction (XXI) terms, respectively. For excitation, where E(t) is an ultrashort optical pulse, these two terms have a very different temporal behavior. In particular when Eq.(I,11) is solved in power expansion of E(t) one can clearly see that the XXI contribution appears **delayed and out of phase** with that of the PSF term! Finally let us note that the XXI term has the same form as the term introduced by Ginzburg and Landau to describe the mechanism that, close to the transition temperature, drives metals toward a superconducting state. In the case of small excitation densities where $n \simeq |\psi|^2$, we can cast Eq.(I,11b) in the form,

$$\frac{\partial}{\partial t}\psi = -i(\Omega - i\Gamma)\psi + i\mu E - i\frac{|\psi|^2}{\psi_s^2}\mu E - iV|\psi|^2\psi, \tag{I,12}$$

where ψ_s is a "saturation" parameter. This equation was extensively discussed in Ref. (5) and used in Ref. (9). To close this analysis, let us mention that the polarization density associated with $\psi(t)$ is;

$$p(t) = \frac{P(t)}{L^3} = |\phi(r=0)|^2 \mu^* \psi(t), \tag{I,13}$$

where L is the box-normalization length.

III)Amplitude and Phase Measurements

The simplest coherent wave-mixing configuration is that of two beam four-wave-mixing (FWM). In such a configuration two ultrashort laser pulses, labeled pulse-2 and pulse-1, separated by a time delay $\Delta t = t_2 - t_1$, and propagating in the directions k_2 and k_1, interfere in a sample to generate a transient grating, which diffracts photons into the

background-free direction $k_s = 2k_2 - k_1$. In the case of homogeneously broadened two level systems the FWM-signal is emitted immediately after the second pulse. It originates from the natural decay of the component of the nonlinear polarization P(t), which emits in the direction k_s, and corresponds to free induction decay (FID).[14] For inhomogeneously broadened lines, the FWM-signal is delayed by Δt after the second pulse and corresponds to a "photon echo". To establish that the FWM-signal comprises of two phase shifted contributions, we are faced with the difficult problem of amplitude and the phase recovery of a signal. To achieve this goal we have used a combination of five measurements to determine five quantities: the time integrated and time resolved intensities, the power spectrum, the interferometric autocorrelation and crosscorrelation with a reference laser pulse. Taken separately, each one is insufficient to retrieve the signal amplitude and phase. All together they give complementary information that allows a good characterization of these two parameters. [8-10] In particular, since the interferometric autocorrelation does not give directly the phase of the FWM signal, we analyze the interferometric data in the following way. For each delay, Δt, we measure the dynamic fringe-spacing, i.e. the number of interferometric fringes during the interferometer delay τ, $FS(\tau)$, for the FWM signal **and**, $FSL(\tau)$ for the laser pulse passing through the same experimental setup and the sample Sapphire-holder but missing the sample itself. The Differential-Fringe-Spacing defined as: $DFS(\tau) = FSL(\tau) - FS(\tau)$ is then determined numerically. For precise calibration, the laser was operated CW, thus providing a reference frequency which was used to analyze the laser autocorrelation when operated mode-locked. The $DFS(\tau)$ sign is determined by measuring the cross-correlation with the laser. If the phase of the FWM signal is a constant or has a linear

time dependence, the DFS(τ) corresponds exactly to the phase difference between the laser and the signal. In the most general case and in the absence of other information, there is no simple mathematical relationship between the DFS(τ) and the phase difference. In our experiments, however, we also know the FWM signal intensity temporal profile and power spectrum, which are smooth and well behaved. We have numerically checked numerous examples which confirm that in this case the DFS(τ) reproduces faithfully the phase difference with the reference.

Excitonic resonances in semiconductors are usually inhomogeneously broadened at low temperatures. In QW-structures, however, the quantum confinement in ultrathin layers, narrower than the bulk Bohr radius, stabilizes the quasi-2D excitons up to room temperature.[1] Collisions with the large population of thermal-phonons homogenize the resonances and shorten their dephasing time. We have investigated two samples consisting respectively of 47 periods of 98Å GaAs QWs and 96Å $Al_{0.3}Ga_{0.7}As$ barrier layers and of 50 periods of 95Å GaAs QWs and 45Å $Al_{0.3}Ga_{0.7}As$ barrier layers. The output of a mode-locked Ti:Sapphire laser, delivering extremely stable $\simeq$ 70-100fs transform-limited Gaussian pulses at 88 MHz. It was tuned close to the heavy hole exciton resonance, $\omega_L \simeq \Omega_{hh}$, and split into three beams. Two of these beams were used to generate the FWM-signal. This signal could be detected directly as a function of Δt using a slow detector in the conventional way. Alternatively, for a fixed Δt, it could be directed in a Michelson interferometer for the autocorrelation measurements. For the power spectra measurements the signal was directed onto a spectrometer and detected by an optical multichannel analyser. In order to time-resolve the amplitude of FWM-signal, for every Δt, the light emitted in the direction k_s was cross-correlated with the third laser

beam by sum frequency generation in a highly transparent nonlinear crystal. This cross-correlation determined the temporal-profile of the FWM-signal vs the absolute time, t. Finally by placing the whole FWM set up inside a Mach-Zender interferometer, the interferometric correlation with the laser could be determined.

In Figure (1) we present time resolved intensity vs absolute time, t, for a series of the time delays Δt, measured with a laser intensity such that the total (generated by both pulses) exciton density is $N_x \approx 10^{12}cm^{-2}$. The laser pulse duration was 78±3fs. The weaker pulse-1 acts at $t = 0$ and the stronger pulse-2 acts at $t = \Delta t$. Clearly, the time traces are asymmetric both in t and Δt. For all our measurements we have verified from the position of the maximum that the FWM-signal is emitted immediately after the second pulse. This behavior confirms that the exciton transition is predominantly homogeneously broadened at room temperature and therefore, that the FWM-signal corresponds to a free-induction decay. Furthermore, the self-consistency of the data was checked by numerically integrating the time resolved intensity vs t, for each Δt and comparing the result to the time integrated intensity measured with a slow detector vs Δt. Again, the agreement is excellent.

In Figure (2) we display the temporal profile of (a) the time resolved intensity vs absolute time t at $\Delta t = 0$ and (b) the time integrated intensity vs Δt, for two exciton densities, $N_x \approx 10^{11}cm^{-2}$ and $N_x \approx 4\times10^{11}cm^{-2}$. The laser pulse duration was (98±2)fs. Since the relevant information is contained in the lineshape, the two curves have been normalized to unity and the unrelated time-axes have been shifted to bring the maxima into coincidence. The difference between the two profiles is evident: the former is clearly

broader than the latter, with a slower rising edge and a significantly non-exponential trailing edge. This difference is density dependent and shows up noticeably on the trailing side of the profiles. Within a Δt series the total exciton density is constant and, therefore, all the time resolved traces are expected to have similar lineshapes, although their height depends on Δt. This is indeed what is observed at low densities, $N_x \approx 10^{11} cm^{-2}$. At moderate density, $N_x \approx 2\text{–}4 \times 10^{11} cm^{-2}$, noticeable changes in the temporal profile are seen within a Δt series. In particular the sign of Δt is found to influence the temporal lineshape.

In order to be more quantitative, we have solved Eq. (I,12) numerically, for the nonlinear polarization, $P^{(3)}(t,k_s)$, radiating in the direction k_s, using Gaussian laser pulses with a duration corresponding to that of our laser and accounting for the effect of upconversion in the time-resolved measurement. This model involves only two fitting parameters: the exciton dephasing time, T_2, and the ratio of the two nonlinearities $R = V\psi_s^2$. We impose on the fit the severe constraint that all curves in a Δt series must have the same origin of the absolute time t and a constant calibration. We find that it is impossible to fit the data with such a constraint if we retain only the PSF term. An excellent fit is obtained, however, if both the XXI and PSF contributions are considered. This is shown in Figure (3), where we present the fit of the temporal profiles at low densities, $N_x \approx 10^{11} cm^{-2}$. The dashed-dotted lines give the PSF contribution, the dashed lines give the XXI contribution, and the smooth solid lines give their sum. The contribution of the XXI to the total energy of the pulse emitted by the sample dominates the emission. It is ≈ 2.2 larger than that due to PSF. As the total exciton density is increased, the XXI contribution is reduced by screening as shown in Figure (4).

Interestingly, we find that it dominates as long as the exciton density does not exceed the exciton saturation density in the sample, $N_s \approx 3\times10^{11}cm^{-2}$.[1] When this critical density is surpassed, the XXI contribution decreases very rapidly and becomes negligible at high densities.

As mentioned above, at low density both T_2 and R remained approximately constant, for all the TRS fits within a single Δt series. At moderate densities, however, this was not found to be the case within a single Δt series (i.e. fixed N_x); both T_2 and R had to be varied to fit the data. These observations can be understood in terms of the well established dynamics of excitons in quantum wells at room temperature.[1] Consider first the case of a total excitation density low enough that photo-generated excitons are the in bound state (binding energy $\approx$ 10meV for $\approx$ 100Å QW) and are spatially well separated. They interact effectively via the Coulomb potential and their dephasing time is determined by phonon collisions. Their environment is independent of the instantaneous density determined by the order in which the laser pulses arrive in the sample (i.e. Δt); therefore, T_2 and R are constant. At moderate densities, however, when the strongest pulse-2 arrives first in the sample, it generates a substantial number of excitons in the bound states. They are ionized by collisions with the energetic thermal phonons (phonon energy $\approx$ 36meV for GaAs), in $\approx$ 100–200fs, generating e-h pairs in scattering states with a significant excess energy ($\approx$ 25meV).[15,16] The charged carriers, in turn, both shorten the relaxation time, T_2, owing to their larger effects on the neutral bound states,[17,18] and screen the Coulomb potential. For the reverse time ordering, i.e. when the weaker pulse-1 arrives first, less e-h pairs are generated by the first pulse, the effects described above are less pronounced, and the sample remains closer to steady state

during the FID emission. Finally, at very high densities, the band gap renormalizes so much during the laser pulses that the excitons are generated in scattering states, giving free e-h pairs immediately. They, of course, shorten the relaxation time below the experimental resolution. More importantly, however, they screen the Coulomb potential to the point that the XXI contribution to the emission is eliminated, see Figure (4). The fits also show that the maximum of the time resolved intensity is delayed with respect to the second pulse. We found that the delay is of the order T_2. This indicates that the time required to **establish** the coherent polarization wave within the sample (rise-time of the emission) is directly related to the dephasing time T_2 which is usually associated only with the negative interferences that produce the signal decay. As the exciton density increases further, the time resolved and time integrated profiles become more similar. Finally, at very high densities, $N_x \approx 10^{12}$–$10^{13}cm^{-2}$, where the band gap renormalization has completely washed out the exciton resonances, the two profiles become of the order of the laser pulse and are beyond our resolution. Then, the profile of all the traces of a Δt series become similar again.

The power spectra of the FWM signal and of the laser are shown in Figure (5) for four densities, $N_x \approx 3\times10^{9}cm^{-2}$, $1.2\times10^{10}cm^{-2}$, $6\times10^{10}cm^{-2}$ and $3\times10^{11}cm^{-2}$, when the laser is tuned slightly below the heavy hole exciton $\omega_L < \Omega_{hh}$. At very low exciton densities, $N_x \approx 3\times10^{9}cm^{-2}$ the FWM power spectra essentially reproduce the line shape of the exciton resonances within the laser spectra. The line shape is asymmetric, and exhibits only one resonance, As the exciton density is increased the FWM power spectra evolves toward that of the laser and becomes almost indistinguishable from it at the highest density shown in Figure (5). Figure (6) shows similar data obtained for a laser

tuned slightly above the heavy-hole exciton $\omega_L > \Omega_{hh}$, which excites also the light-hole resonance. Two unequal peaks are present at low densities. They evolve toward a single and broader peak, almost in coincidence with the laser, as the density increases. The low-density line shapes in the two figures suggest, by Fourier-transform, dynamic nonlinear shifts of the FWM frequency during a single pulse.

Figure (7) shows the $\Delta t = 0$ autocorrelation traces and DFS(τ) for (a) the mode-locked laser (calibrated to the reference frequency of the laser operated CW), (b) the low-density FWM signal and (c) the high-density FWM signal for a $\omega_L < \Omega_{hh}$ excitation corresponding to Figure (5). Figure (8) shows the same quantities when $\omega_L > \Omega_{hh}$ as in Figure (6). In both cases the high-density autocorrelation envelopes of the FWM signal are of the order of that of the laser and the DFS(τ) indicates that the FWM instantaneous frequency presents no significant difference with that of the laser. Conversely the low-density the envelopes are much longer than that of the laser and, more importantly, the DFS(τ) shows significant nonlinear frequency shifts. For $\omega_L < \Omega_{hh}$, the low-density DFS(τ) starts with a positive linear variation. The slope corresponds exactly to the difference in frequencies between the laser and the principal peak seen in the FWM power spectrum of Fig. (5a). Then for 300fs<t<450fs the DFS(t) slope vanishes, indicating that during the pulse, the instantaneous frequency shifts toward that of the laser. This nonlinear phase dynamic is consistent with the power spectra of Fig. (5). In particular, the power spectrum of Fig. (5a), besides a main peak at the hh-exciton frequency, exhibits an asymmetric low frequency tail which extends well into the laser spectra. For $\omega_L > \Omega_{hh}$, again the high-density DFS(τ) has a zero slope showing that the FWM frequency is essentially that of the laser. Conversely, the low-density DFS(τ) also

starts with a zero slope and then exhibits a negative variation with a curvature. This indicates that, in this case, the FWM frequency starts at the same frequency as the laser but is quickly dominated by a component below the laser central frequency. The dynamics of the instantaneous frequency, however, is complicated and does not correspond to a simple linear variation. Again this is consistent with the power spectrum of Fig. (7a), which shows strong but unequal contributions from both excitons. In order to further explore this case we have adjusted the excitation frequency, $\omega_L \simeq \Omega_{lh}$, and intensity to obtain hh-exciton and lh-exciton contributions of roughly the same weight in the FWM power spectrum, as shown in Fig. (9a). In this case, the interferometric autocorrelation, Fig. (9b) clearly shows several interference patterns which are in excellent agreement with the separation of the two peaks of the FWM power spectrum of Fig. (9a). In order to establish that the observed effect corresponds to the quantum beats of an homogeneous system and not to polarization interferences from independent systems we have applied the method of Ref. (19). We verified that the asymmetric features seen in the interferometric cross-correlation for various time delays, vary as Δt and not as $2\Delta t$. Quantum beats between hh- and lh-excitons have been observed recently as modulations of the decay of FWM signal intensity[20,21]. The new information provided by the interferometric techniques is shown in Fig.(9c) where the DFS(τ) is depicted. It starts with a zero slope showing that the FWM frequency is the same as that of the laser, $\omega_L \simeq \Omega_{lh}$. Then it exhibits a negative curvature showing a change toward a lower frequency. At around $\tau \simeq 120$fs, the DFS(τ) experiences a sudden phase shift of π, before resuming its negative variation. The position of the π-shift corresponds to the middle to the first node in Fig. (9b). It occurs over a very short interval of about 10

optical fringes. This is shown in the lower left part of the figure where about a dozen of the fringes close to the center and close to the node of the autocorrelation trace have been expanded. The half-fringe shit over eleven fringes is clearly seen. The signal to noise ration is excellent. Since one fringe corresponds to 2.8fs and the measurement is performed with a calibration of 21 stepper motor steps per fringe or an accuracy of $\simeq 0.14$fs.

IV) Conclusion

The time resolved amplitude measurements are very well explained by the model based on a single-resonance-excitaion approximation of the Semiconductor Bloch equations. They show that not only there is a XXI contribution to the nonlinear response, but that, in fact, this contribution dominates over the PSF one whenever the Coulomb interaction is not screened.

The phase measurements provide much more delicate information on the dynamics of the instantaneous frequency of the FWM signal. The experimental observations obtained in the case of single-resonance contribution to the FWM, can be explained qualitatively in terms of the two-band Semiconductor Bloch equation. However since the exciton linewidth and the ultrashort pulse laser spectrum are both rather broad the detail of their overlap has to be carefully accounted for. From the purely experimental point of view, the consistency of the power spectra, Figure (5), and autocorrelation differential-fringe-spacing, Figure (7), measurements are excellent. The case where two resonances contribute to the FWM is more difficult to treat theoretically. It is necessary to consider three-band semiconductor Bloch equations with two valence bands. In this case one finds

two families (heavy-holes & light-hole) of excitons. Each one possesses "internal" Coulomb and Pauli nonlinearities, but, furthermore, they are coupled via these two mechanisms as well. The coupling of the hh-X and lh-X families by Pauli exclusion originates naturally from the fact that they share the same conduction bands. Hence once an exciton of one family is created the transitions to the conduction band for the other family is affected. The Coulomb coupling between hh-X and lh-X originates from the inter-valence band transitions which provide an additional transition channels between the conduction band and either one of the valence bands.[24] This model implies that the inter-valence band transitions can be driven by excitation near the fundamental gap and emit THz radiation. This effect has been recently observed.[25]

ACKNOWLEGEMENT:

This work was performed in collaboration with M.-A. Mycek, S. Weiss, J.-Y. Bigot and R.G. Ulbrich.

It was supported by the Director, Office of Energy Research, Office of Basic Energy Sciences, Division of Materials Sciences of the US Department of Energy, under Contract No. DE-AC03-76SF00098.

REFERENCES

1. S. Schmitt-Rink, D.S Chemla, D.A.B. Miller, Adv. in Phys. 38, 89 (1989)

2. S. Schmitt-Rink, D.S. Chemla, Phys. Rev. Lett. 57, 2752 (1986). and S. Schmitt-Rink, D.S. Chemla, H. Haug, Phys. Rev. Lett. B37, 941 (1988).

3. K. Leo, M. Wegener, J. Shah, D.S. Chemla, E.O. Göbel, T.C. Damen, S. Schmitt-Rink, and W. Schäfer, Phys. Rev. Lett. 65, 1340 (1990);

4. M. Wegener, D.S. Chemla, S. Schmitt-Rink, and W. Schäefer, Phys. Rev. A 42, 5675 (1990).

5. S. Schmitt-Rink, S. Mukamel, K. Leo, J. Shah, and D.S. Chemla, Phys. Rev. A 44, 2124 (1991).

6. W. Schäfer, F. Jahnke, and S. Schmitt-Rink, Proceeding of the International Meeting on Optics of Excitons in Confined Systems, Gardini Naxos, Italy 1991, Inst. Phys. Conf. Ser. No. 123, and submitted to Phys. Rev. Lett.

7. A.V. Kuznetsov, Phys. Rev. B44, 8721 and 13381 1991-II

8. M.-A. Mycek, S. Weiss, J.-Y. Bigot, S. Schmitt-Rink, D.S. Chemla, Appl. Phys. Lett. 60,

9. S. Weiss, M.-A. Mycek, J.-Y. Bigot, S. Schmitt-Rink, D.S. Chemla, Phys. Rev. Lett. 69, 2685 (1992)

10. J.-Y. Bigot M.-A. Mycek, S. Weiss, R.G. Ulbrich, D.S. Chemla, Phys. Rev. Lett. 70, 3307 (1993)

11. See for example: "Optical Nonlinearities and Instabilities in Semiconductors" H. Haug ed. Academic Press New York 1988

12. M.-A. Mycek, J.-Y. Bigot, and D.S. Chemla, to be published

13. T. Yajima,and Yoichi Taira, J. Phys. Soc. Jap. 47, 1620 (1979)

14. See for example: L. Allen and J.H. Eberly, "Optical Resonances and Two Level Atoms" (Wiley, New York 1975)

15. W.H. Knox, C. Hirlimann, D.A.B. Miller, J. Shah, D.S. Chemla, and C.V. Shank, Phys. Rev. Lett. 56, 1191 (1986).

16. W.H. Knox, D.S. Chemla, G. Livescu, J.E. Cunningham, and J.E. Henry, Phys. Rev. Lett. 61, 1290 (1988), W.H. Knox, in "Hot Carriers in Semiconductor Nanostructures", J. Shah ed. Academic Press (1992).

17. L. Schultheis, M.D. Sturge, and J. Hegarty, Appl. Phys. Lett. 47, 995 (1985).

18. L. Schultheis, J. Kuhl, A. Honold, C.W. Tu, Phys. Lett. 55, 1635, (1986)

19. M. Koch, J. Fedman G. von Plessen, E.O Göbel, P. Thomas and K. Köhler Phys. Rev. Lett. 69, 3631 (1992)

20. K. Leo, J. Shah, E.O. Gvbel, T.C. Damen, S. Schmitt-Rink, W. Schäfer, J. Muller, K. Köhler, Phys. Rev. Lett. 66, 201, (1991) and Mod Phys. Lett. B5, 87, (1991)

21. E.O. Göbel, K. Leo, T.C. Damen, J. Shah, S. Schmitt-Rink, W. Schäfer, J. Muller, K. Köhler, Phys. Rev. Lett. 64, 1802, (1990)

22. M-A Mycek, J-Y. Bigot, S. Weiss, R.G Ulbrich, D.S. Chemla to be published

23. P.C.M. Planken, M. C. Nuss, I Brener, K. Gossen, M. S. C. Luo, S.L. Chuang, L. Pfieffer Phys. Rev. Lett. 69, 3800 (1992).

FIGURE CAPTIONS

Figure (1): Time resolved four wave mixing signal vs absolute time t, for a series of Δt and a total exciton density $N_x \approx 10^{12}cm^{-2}$.

Figure 2: Comparison of the temporal profile of (a) the time resolved signal at $\Delta t = 0$ and (b) the time integrated signal, for for two exciton densities, $N_x \approx 10^{11}cm^{-2}$ (left) and $N_x \approx 4\times10^{11}cm^{-2}$ (right).

Figure (3): Fit of the time resolved intensity profiles at various Δt for $N_x \approx 10^{11}cm^{-2}$, using the model discussed in the text. The dashed-dotted lines give the Pauli exclusion contribution, the dashed lines give the exciton-exciton interaction contribution, and the smooth solid lines corrspond to their sum.

Figure (4): Time resolved intensity profiles and theoretical fit for (a) $N_x \approx 10^{13}cm^{-2}$ (b) $N_x \approx 10^{12}cm^{-2}$ (c) $N_x \approx 4\times 10^{11}cm^{-2}$ (d) $N_x \approx 2\times 10^{11}cm^{-2}$ (e) $N_x \approx 10^{11}cm^{-2}$, showing the effects of screening on the relative strength of the Pauli exclusion and Exciton-exciton interaction nonlinearities.

Figure (5): Power spectra of the Four Wave Mixing signal and laser spectra for exciton densities, (a) $N_x \approx 3\times10^{9}cm^{-2}$ (b) $N_x \approx 1.2\times10^{10}cm^{-2}$ (c) $N_x \approx 6\times 10^{11}cm^{-2}$ (d) $N_x \approx 3\times 10^{11}cm^{-2}$, when the laser is tuned slightly below the heavy-hole exciton.

Figure (6): Power spectra of the Four Wave Mixing signal and laser spectra for exciton densities, (a) $N_x \approx 4\times10^{9}cm^{-2}$ (b) $N_x \approx 1.2\times10^{10}cm^{-2}$ (c) $N_x \approx 6\times 10^{11}cm^{-2}$ (d)

$N_x \simeq 3\times 10^{11}cm^{-2}$, when the laser is tuned slightly above the heavy-hole exciton.

Figure (7): Interferometric auto-correlation, and Differential- Fringe-Spacing for (a) the laser, (b) the low-density and (c) the high-density FWM signal in the case where the laser is tuned slightly below the heavy-hole exciton. The conditions of (b) and (c) are the same as that of the power spectra (a) & (b) of Figure (5).

Figure (8): Interferometric auto-correlation and Differential- Fringe-Spacing for (a) the laser, (b) the low-density and (c) the high-density FWM signal in the case where the laser is tuned slightly above the heavy-hole exciton. The conditions of (b) and (c) are the same as that of the power spectra (a) & (b) of Figure (6).

Figure (9): (a) Power spectrum, (b) Interferometric auto-correlation, and (c) Differential-Fringe-Spacing of the FWM signal in the case where when the laser is tuned to give contributions of the hh- and lh-exciton of approximately same weights. The lower left figure is a blow up of about a dozen of fringes close to the center and the node of the autocorrelation trace showing how the π-shift occurs over eleven fringes only.

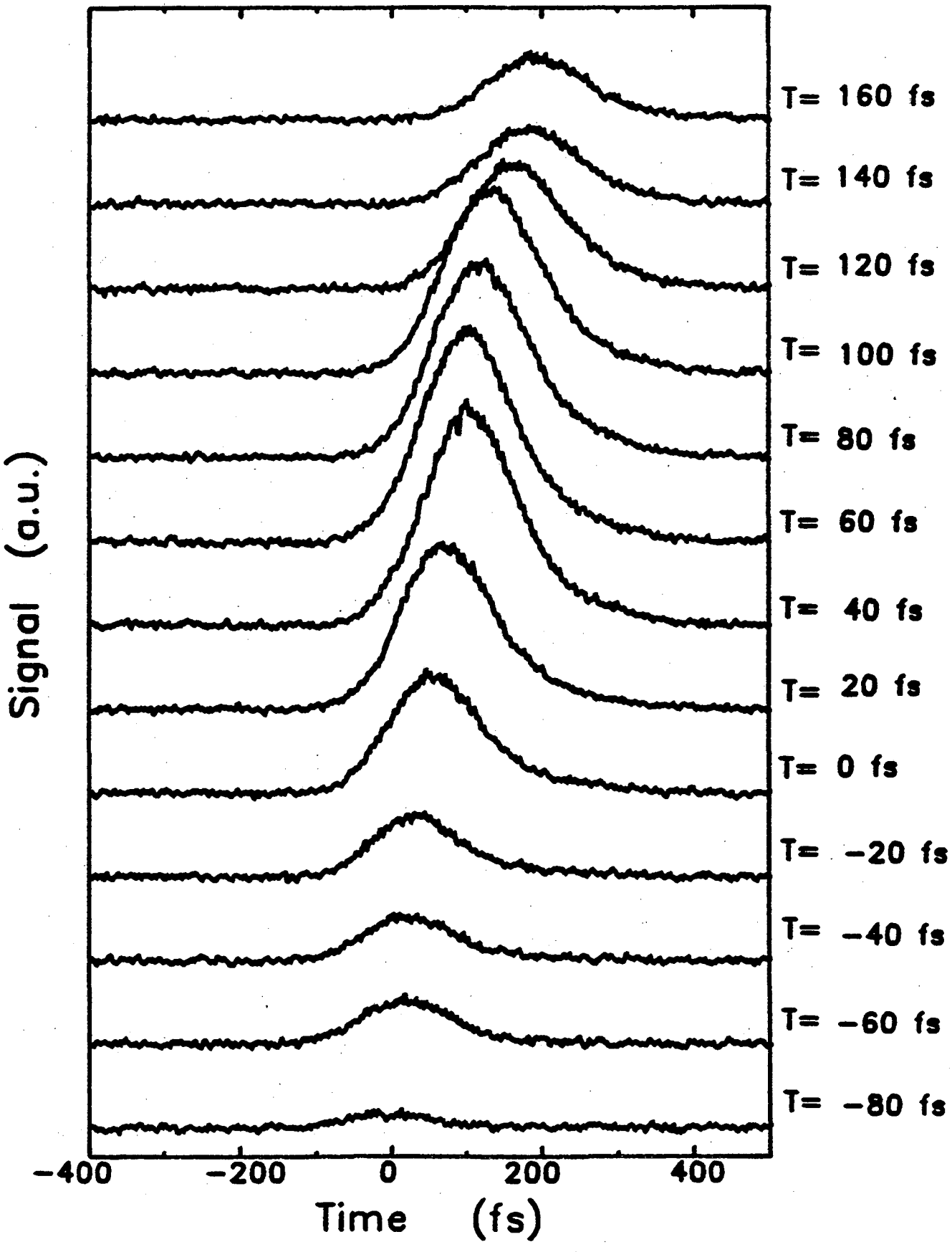
T= 160 fs
T= 140 fs
T= 120 fs
T= 100 fs
T= 80 fs
T= 60 fs
T= 40 fs
T= 20 fs
T= 0 fs
T= -20 fs
T= -40 fs
T= -60 fs
T= -80 fs
Signal (a.u.)
-400
-200
0
200
400
Time (fs)

Diffracted Signal (a.u.)
(a)
(b)
200 fs
time (fs)

Diffracted Signal (a.u.)
(a)
(b)
200 fs
time (fs)

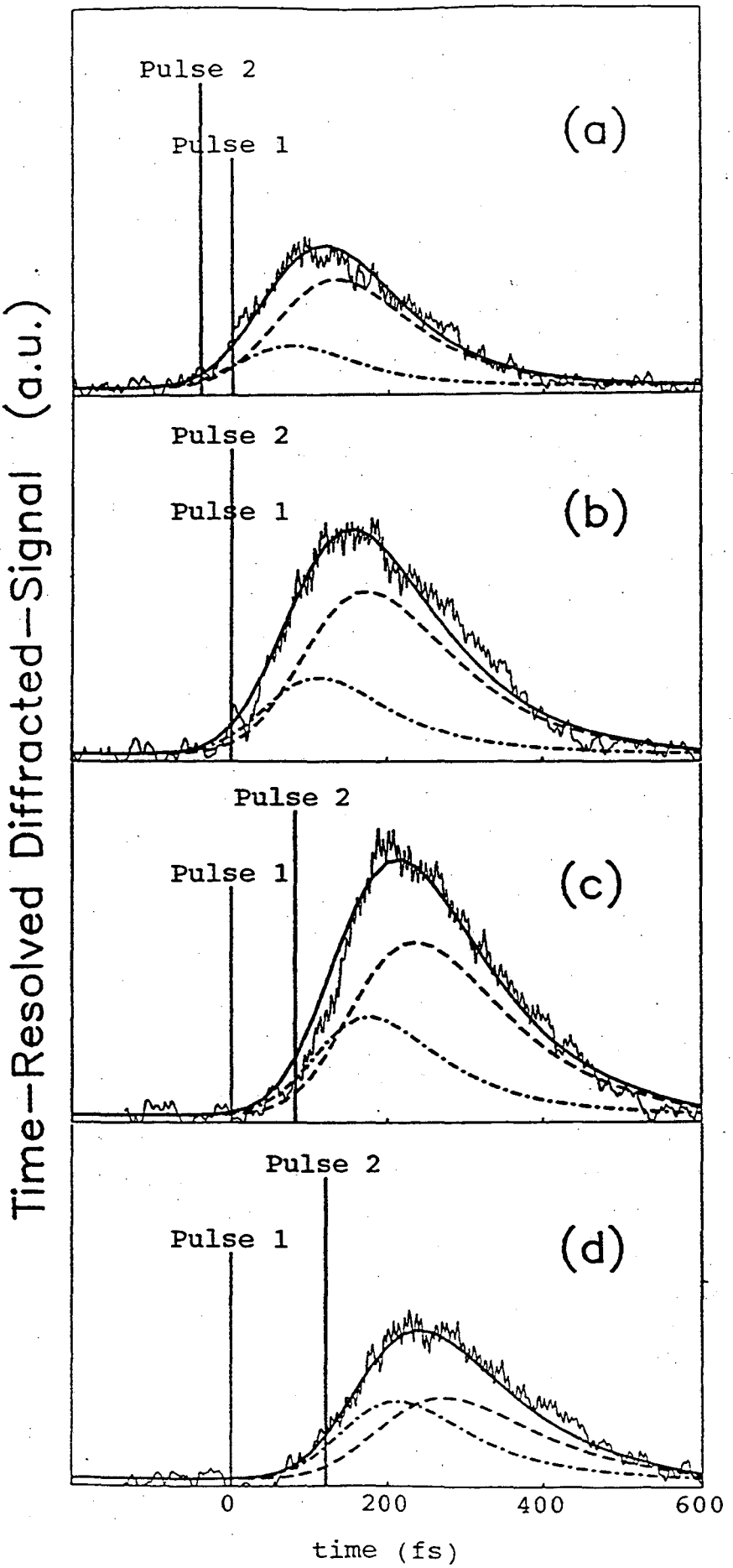
Pulse 2
Pulse 1
(a)
Pulse 2
Pulse 1
(b)
Pulse 2
Pulse 1
(c)
Pulse 2
Pulse 1
(d)
Time-Resolved Diffracted-Signal (a.u.)
0
200
400
600
time (fs)

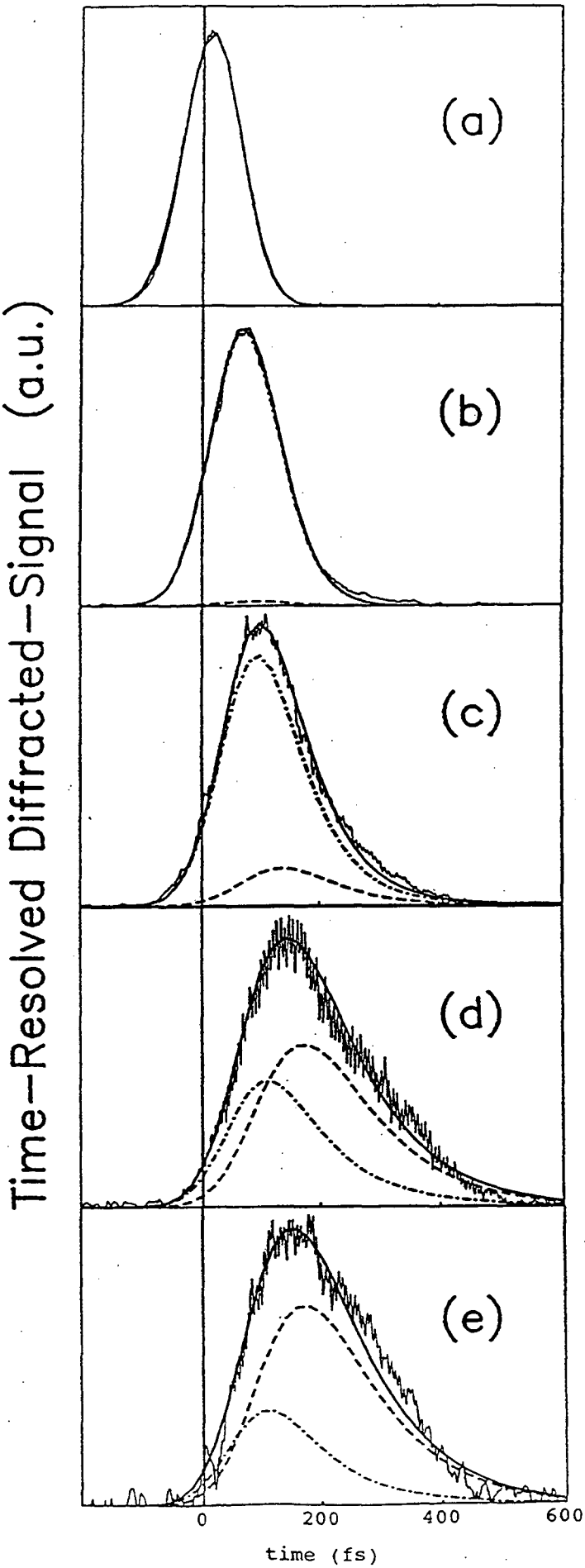
Time-Resolved Diffracted-Signal (a.u.)
(a)
(b)
(c)
(d)
(e)
0
200
400
600
time (fs)

Power Spectra Below Resonance excitation

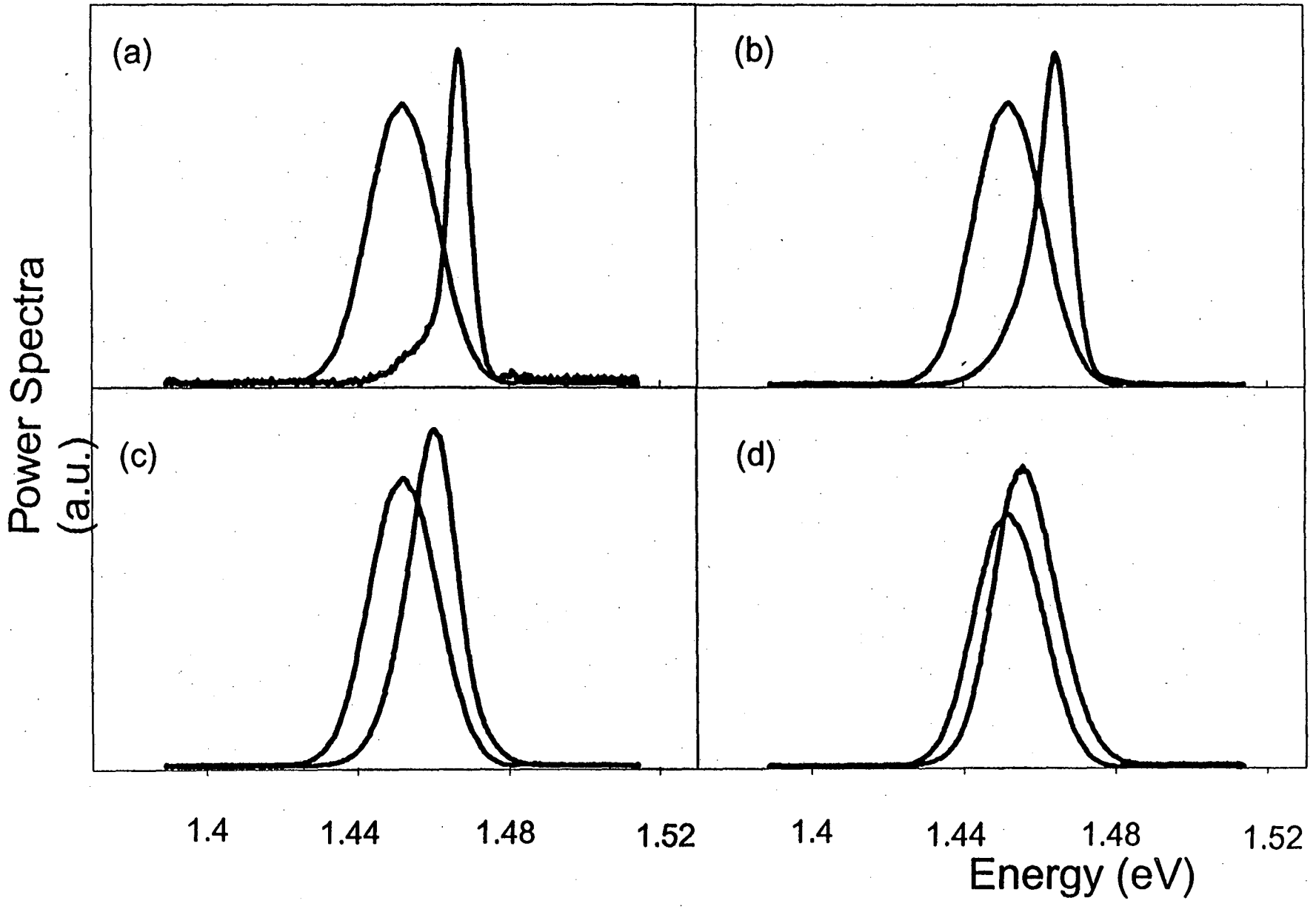

Power Spectra Above Resonance Excitation

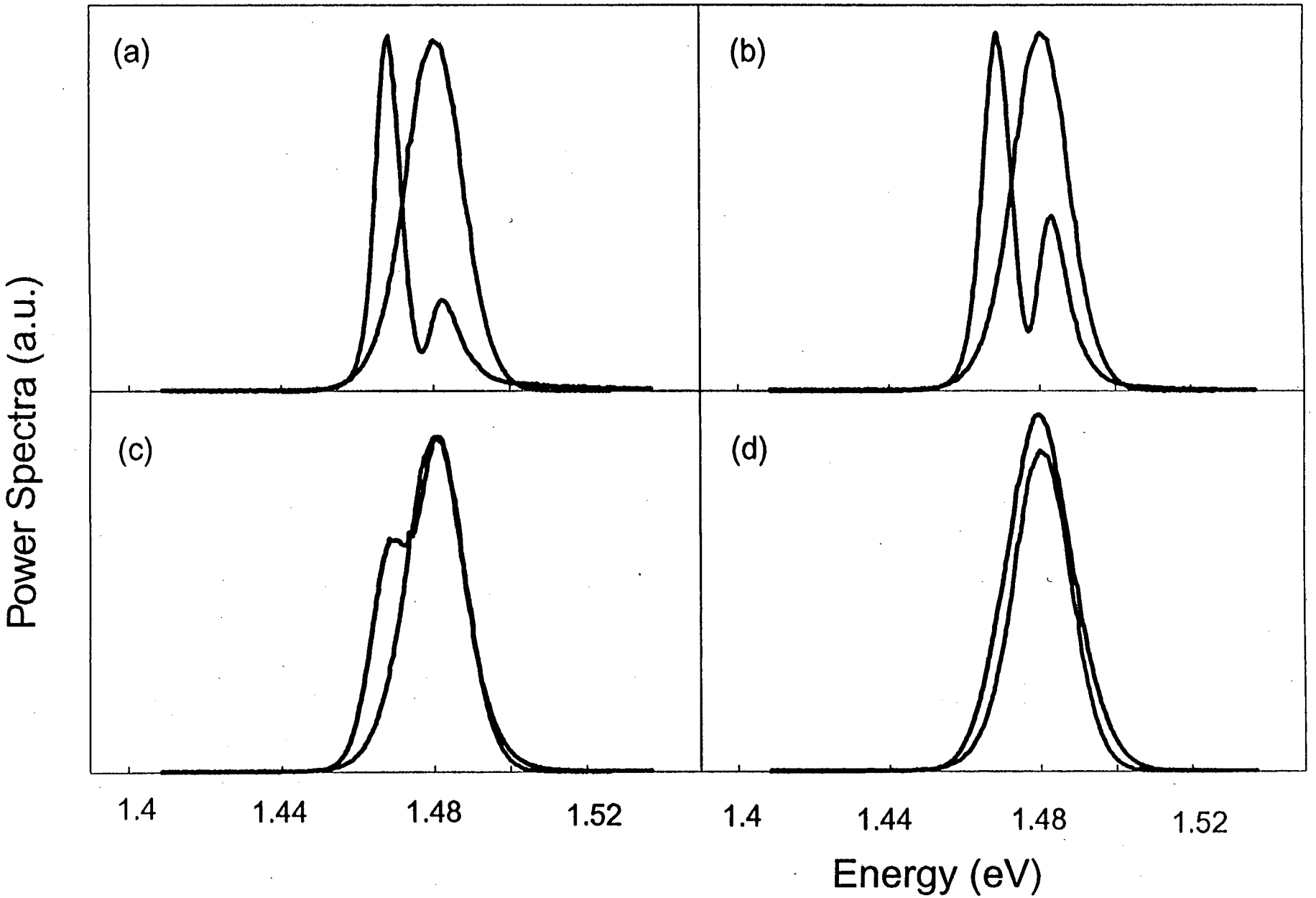

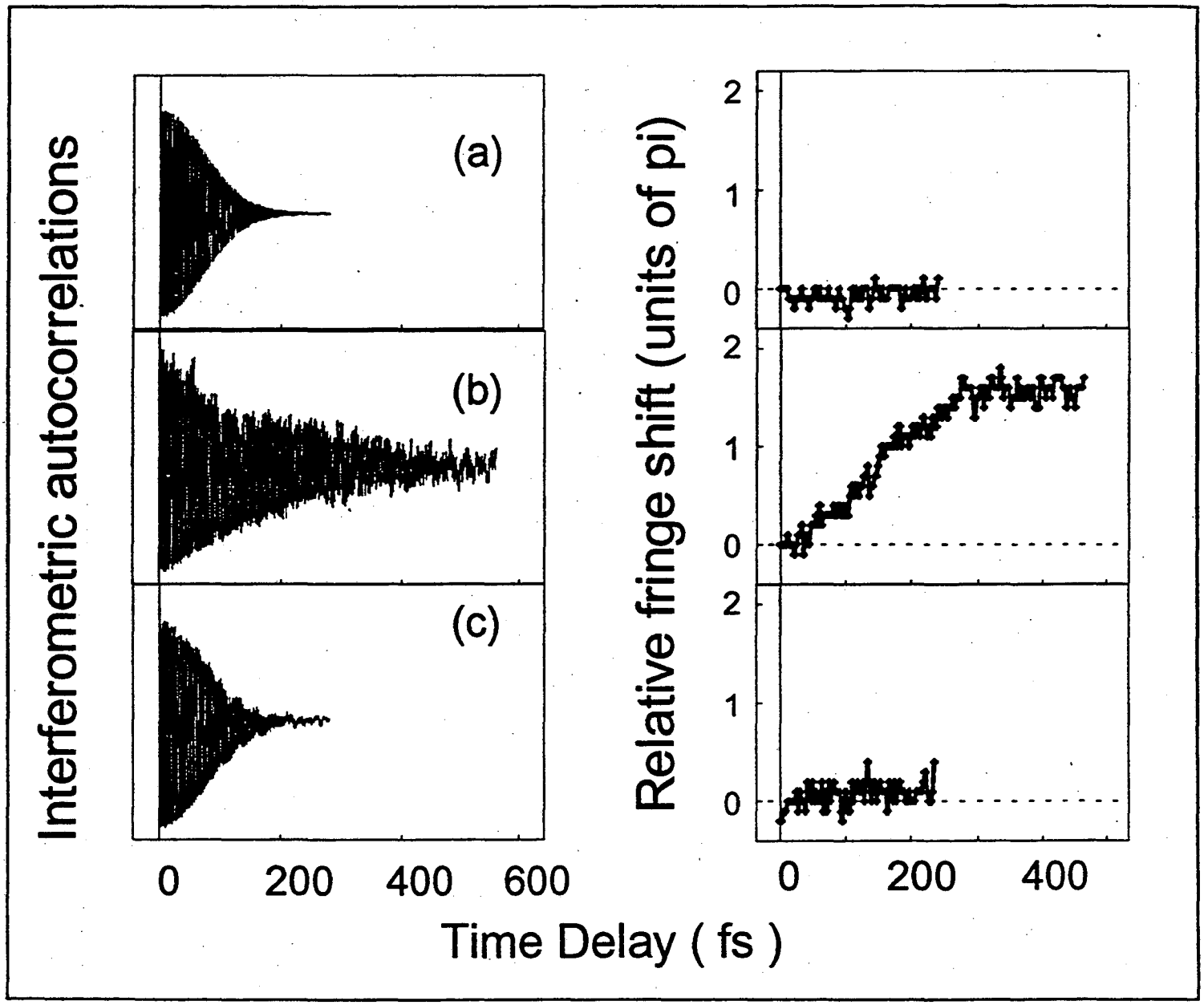
Interferometric autocorrelations
(a)
(b)
(c)
0
200
400
600
Relative fringe shift (units of pi)
2
1
0
2
1
0
2
1
0
0
200
400
Time Delay (fs)

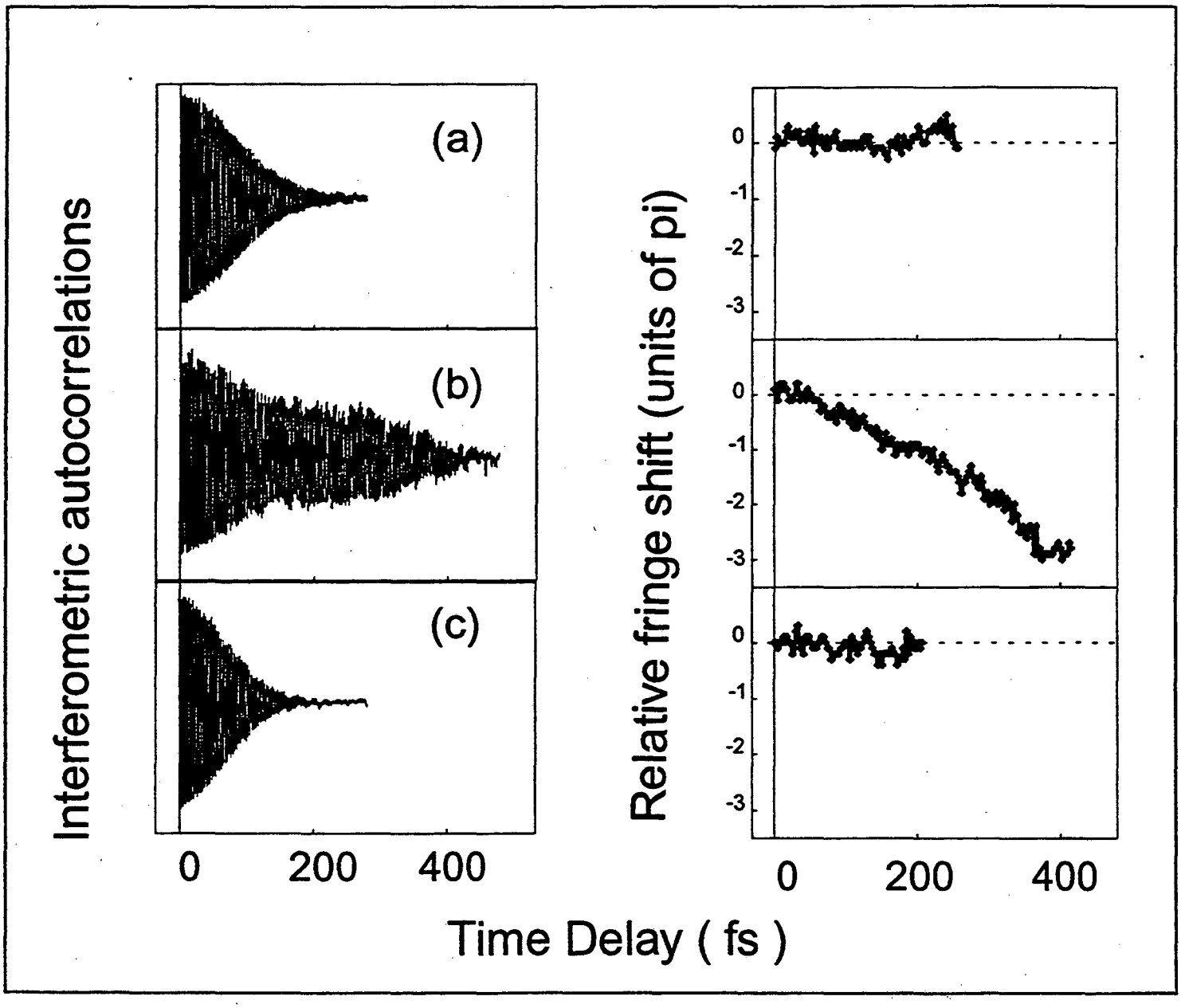
Interferometric autocorrelations
(a)
(b)
(c)
0
200
400
Relative fringe shift (units of pi)
0
-1
-2
-3
0
200
400
Time Delay (fs)

(a)
Power spectra (a.u.)
1.44
1.48
1.52
Energy (eV)
(b)
interferometric
autocorrelation
0
160
320
480
Time Delay (fs)
(c)
relative fringe
shift (units of pi)
0
-1
-2
0
80
160
240
Time Delay (fs)

LAWRENCE BERKELEY LABORATORY
UNIVERSITY OF CALIFORNIA
TECHNICAL INFORMATION DEPARTMENT
BERKELEY, CALIFORNIA 94720